ADVANCED MATERIALS TECHNOLOGIES
www.advmattechnol.de

# Laser Writing of Eutectic Gallium–Indium Alloy Graphene-Oxide Electrodes and Semitransparent Conductors

*Alexandre Chambel, Afsaneh L. Sanati, Pedro Alhais Lopes, Timur Nikitin, Rui Fausto, Aníbal T. de Almeida, and Mahmoud Tavakoli**

**Graphene encapsulated liquid metal particles is a novel and promising class of biphasic composite, with application in the next generation of electronic devices. Here, rapid, low-cost, and scalable fabrication of solution processed large area rGO@EGaIn electrodes is demonstrated. rGO@EGaIn solution is first deposited over the substrate through spray coating, and then processed through a low-cost laser (master oscillator power amplifier (MOPA)). This allows simultaneous reduction, thinning, ablation, and high resolution patterning of the deposited films. Surprisingly, it is found that by adjusting the laser parameters, it is possible to make semitransparent conductors via laser thinning of the films. Scanning electronic microscopy (SEM) and energy dispersive X-ray spectroscopy (EDS) spectroscopy confirm that although the rGO/EGaIn weight ratio is only ≈0.08, the composite has a considerably different microstructure compared to the eutectic gallium–indium alloy (EGaIn) particles alone. Graphene oxide (GO) protects the EGaIn from extreme morphology change under laser irradiation. Therefore, various "shades" of rGO@EGaIn can be fabricated in a single film. This allows development of large electrodes with complex geometries in a few seconds. The conductivity, transparency, and reduction of the laser processed films are characterized by several techniques and an example of application is demonstrated by laser patterning a highly sensitive breath-monitoring sensor.**

## 1. Introduction

Graphene is arguably the most studied carbon based material in the last decade.[1] This is due to its high carrier mobility,[2] transparency,[3] and mechanical strength.[4] Graphene-metal composites received an increasing attention in the recent years, as these composites exhibit enhanced electrical, mechanical, and chemical properties for a diverse range of applications. For example a GO-AgNW composite, were studied as a flexible alternative for ITO (indium tin oxide) conductors.[5] Au-GO composites have been used in biosensors, biodevices and DNA sequencing applications, whereas, for instance, Si-GO and Co-GO are promising for Li-ion battery fabrication.[6] Previous works on laser patterning of GO (graphene oxide) includes using continuous-wave (CW)[7] or pulsed lasers with femto to microsecond pulsewidth.[8–10]

On the other hand, Liquid Metals (LMs), such as EGaIn (eutectic gallium–indium alloy), have received special attention in the past few years, due to their unique liquid-state properties, fluidic behavior, non-toxicity,[11] metallic conductivity,[12] low viscosity,[13] "moldability", self-healing,[14] the possibility of fabrication of micro/nano particles,[15] and the emerging techniques for digital fabrication of EGaIn based electronics.[16] Application of EGaIn micro and nanomaterials has been demonstrated for soft electronics,[17–20] and health monitoring.[22,23] Composites of liquid metal with elastomers,[24] and LM-Ag elastomer composites[25] have been demonstrated as soft and stretchable materials in electronics, and thermal conducting elastomers. EGaIn nanoparticles (NPs), with their gallium oxide shell/liquid core assembly, have been reported as a laser sensitive material, inducing the production of highly conductive patterns on soft substrates like PDMS (polydimethylsiloxane). The laser ruptures the nanometric $Ga_2O_3$ semiconductor shell around the EGaIn particles, resulting in formation of conductive EGaIn micro paths.[26,27] Furthermore, UV photolithography of EGaIn microparticles dispersed in a photoresist and coated on soft substrates has been reported for micropatterning.[28] More so, direct nanofabrication of EGaIn has also been reported using hybrid lithography techniques (soft and electron-beam lithography) for soft and high density electronic devices.[29] However, laser thinning of such particle films for the fabrication of transparent conductors has not been reported so far.

In the previous year, the GO-EGaIn composite was considered in a few works.[30–32] Unlike the EGaIn droplets, graphene is very stable in a broad range of pH environments,[30] and thus graphene can serve as a protective layer that replaces the

A. Chambel, A. L. Sanati, P. A. Lopes, A. T. de Almeida, M. Tavakoli
Institute of Systems and Robotics
University of Coimbra
Coimbra P-3004-535, Portugal
E-mail: mahmoud@isr.uc.pt

T. Nikitin, R. Fausto
CQC- IMS
Department of Chemistry
University of Coimbra
Coimbra P-3004-535, Portugal

The ORCID identification number(s) for the author(s) of this article can be found under https://doi.org/10.1002/admt.202101238.

**DOI: 10.1002/admt.202101238**

 

natural occurring gallium oxide shell. As we will show in this article, the graphene layer also protects the LM droplets from the rupture under laser generated heat.

Graphene decorated EGaIn particles can potentially combine the advantages of graphene, i.e. high surface area, excellent mechanical and chemical resistance, with the excellent electromechanical properties of liquid metals, e.g. high electrical conductivity. Besides, the solid-liquid interface between the graphene and the liquid metal can enhance the charge transfer within the composite. Therefore, this material has the potential of making a revolution in batteries, supercapacitors and sensors. However, it was challenging to obtain conductive GO@EGaIn electrodes, and deposition along with patterning of circuits based on this material is yet to be demonstrated.

A previous study demonstrated the galvanic replacement of EGaIn/GO frameworks by simple sonication treatment, concluding that GO induces higher electrochemical detection sensitivity for heavy metal ions, such as $Cd^{2+}$ [31] Another study evaluated different solvent possibilities to produce GO encapsulated EGaIn particles, concluding that water is fundamental to allow the chemical interaction between GO and the surface of EGaIn, and that GO shells induce higher stiffness on EGaIn particles.[30] In another work,[32] it was shown that graphene flakes induce the integration of colloidal EGaIn into soft polymeric matrices by promoting cavity formation, through which liquid metal particles enter. They created a flexible composite which resulted in an electrically conductive elastomer after the application of 0.1 MPa of pressure. Further progress in this field requires methods that allow fabrication of conductive electrodes with the desired geometry, using the GO@EGaIn composite.

In this article, we demonstrate for the first time the fabrication of conductive GO-decorated-EGaIn-microcomposite electrodes, using a low-cost MOPA (Master Oscillator Power Amplifier) laser. We further demonstrate that large electrode, and sensing devices with complex geometries and micrometric features can be fabricated using simultaneous laser reduction, patterning, and ablation of spray coated GO@EGaIn composite. Surprisingly, we found that by fine-tuning the laser parameters, it is even possible to fabricate semitransparent conductors. We further demonstrate various "shades" of GO-LM electrodes, using different laser parameters.

This technique can serve as a versatile method for rapid prototyping, and scalable fabrication of laser reduced GO@EGaIn electrodes with micron sized features in few seconds. Unlike previous methods for deposition of graphene and GO, such as CVD (Chemical Vapor Deposition),[33] spin coating,[34] the spray coating technique used in this work allows deposition of large area conductors. Although spray coating is performed manually, the resulting electrodes after laser treatment present an acceptable repeatability in terms of electrical resistance. Therefore, this material composition, and the fabrication method presented in this work, is a step towards scalable and low-cost fabrication of graphene based large area electrodes, sensing devices, and transparent conductors. In addition, we demonstrate a stable suspension of GO@EGaIn, using a GO suspension in water, bulk EGaIn and acetic acid, followed by ultrasonic treatment at low temperatures, and further planetary mixing. The solution prepared in this work is slightly different from the one presented in refs [30,31], as we replaced the HCl acid with the weak acetic acid, which showed good enough behavior for further dispersing the particles in a stable suspension.

Besides, this work is the first report on using a nanosecond, 1064 nm MOPA laser for reduction of a GO based composite. The MOPA laser is a recent low-cost technology that allows pulse width modulation, which is not possible with previous fiber lasers. The influence of laser parameters on the electrical and optical properties of the processed electrodes is thoroughly studied, namely the impact of laser fluence, scanning speed, and pulse width on conductivity and transparency of the laser processed films. As an example of application, we demonstrate the rapid fabrication of an array of interdigital electrodes, and show its application in sensing human breath from a distance of 40 cm. We, expect this technique to be adapted for various applications in sensors, transparent conductors, and energy storage devices.

Finally, through X-Ray diffraction (XRD) analysis, and Raman spectroscopy, and SEM microscopy, we investigated the composition, morphology, and oxide reduction of the composite before, and after laser radiation.

In this article the term rGO@EGaIn refers to reduced graphene decorated EGaIn particle before laser processing. Note that during sonication the GO is partially reduced. To distinguish, we use LrGO@EGaIn to refer to the material after being laser reduced.

Referring to **Figure 1**A, the rGO@EGaIn colloidal solution was obtained by sonicating (≈20 min) 1 g of EGaIn into 20 ml of 0.4% (wt) graphene oxide water solution (Graphenea), with the intermediate addition of 1 ml of acetic acid (0.1 M). It is interesting to highlight that the GO/EGaIn weight ratio is only 0.08. The solution was then mixed for 3 min at 2000 rpm using a planetary mixer (Thinky ARE-250). This results in a suspension of partially reduced GO coated EGaIn particles – Figure 1B). The solution was then spray coated over a substrate (i.e. glass or poly(methyl methacrylate), PMMA), using a spray gun. The sheet resistance of the spray coated samples, prior to the laser reduction was measured to be ≈(30 ± 5) kΩ/sq, which is ≈3 orders of magnitude lower than that of spray coated EGaIn particles prior to the laser reduction. Finally, the spray coated sample was further reduced using a 20 W MOPA laser (JPT).

## 2. Results

### 2.1. Laser Parametrization

To evaluate the influence of different laser parameters (pulse width, power and speed) on LrGO@EGaIn films, we prepared spray coated rGO@EGaIn films on glass, over which we laser reduced 40 squares of 3 $mm^2$ each, using the MOPA laser. Each 4 squares are repetitions of the same parameter, as evidenced on **Figure 2**Bi. Referring to Figure 2Ai, and Figure 2Aii, we first evaluated the role of the laser pulse width. For that, laser power and speed were fixed at 85% and 50 mm/s, respectively; while the pulse width was changed with the frequency according to the pulse width/frequency dependency table provided by the laser manufacturer (table 1 from Supporting Information). This way, the pulse width was increased from 6 to 250 ns; while the frequency was progressively decreased between 350 kHz

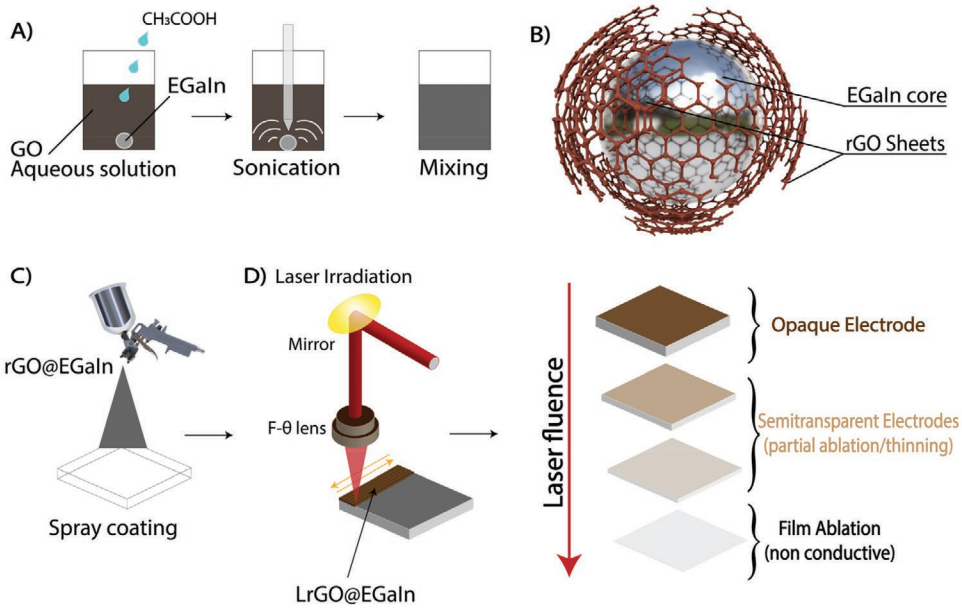


**Figure 1.** Schematic overview of the fabrication of rGO@EGaIn composite, deposition and laser processing: A) composite synthesis via ultrasonic treatment and mixing; B) core-capsule structure of a single rGO@EGaIn particle; C) spray coating on a glass substrate; D) laser irradiation of the rGO@EGaIn films: from laser reduction to total film ablation.

and 40 kHz. No conductivity was measured for the films processed at or above 30 ns (pulse width), as the particles were likely ablated too harshly, with no significant material left. The 9 ns pulse width sample was able to provide the best trade-off between conductivity and transparency. It can be also noticed from Figures 2Ai,Bi) that, although the samples were manually spray coated, the final registered electrical resistance after laser reduction presents repeatable results.

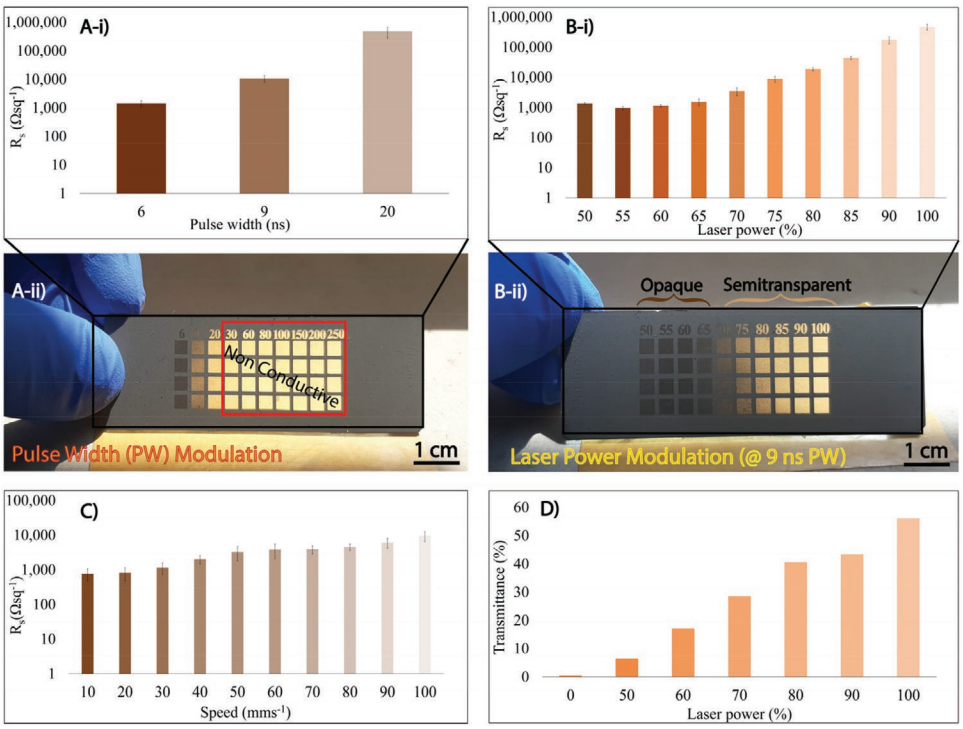


**Figure 2.** Laser parametrization for spray coated rGO@EGaIn films: A-i) Sheet resistance of the films processed at different pulse widths; B-i) Sheet resistance of the films processed at different laser powers; A-ii) a sample showing the different laser marks made at different pulse widths; B-ii) a sample showing the different laser marks made at different laser powers; C) Sheet resistance of the films processed at different laser speeds; D) transmittances of the different films processed at different laser powers.

We then evaluated the laser power – Figure 2Bi,ii– while fixing the pulse width at 9 ns, the frequency at 240 kHz, and laser speed at 50 mm/s. The power was varied between 50 and 100%. Laser fluences were, therefore, varied between 1.19 J/cm$^2$ – 9.95 J/cm$^2$. The sheet resistance increased along with the applied fluence, which happens due to excessive layer thinning of the material, especially for powers above 70%. Nevertheless, both opaque and semitransparent conductive squares could be obtained. Therefore, we selected 70% power for the next samples. Note that, in this work our objective was to reach the best trade-off between transparency and conductivity.

Finally, we varied the laser speed between 10 mm/s and 100 mm/s, in 10 mm/s steps, as shown on Figure 2C. As it can be seen, when the transparency is not important, low laser fluences are enough to reduce the sample, and achieve a sheet resistance below 1 kΩ/sq. The increase in the laser fluence increases slightly the sheet resistance but improves drastically the transparency. Figure 2D shows the dependency between the transmittance and the laser power. At 100% power, the optical transparency reaches to over 50%. Note that the increased sheet resistance does not mean that the actual electrical conductivity of the material is also decreasing. Instead, it only indicates that a material thinning is occurring, which results in higher sheet resistance. The material thinning subject is further discussed based on the results shown in **Figure 3**.

### 2.2. SEM/EDS and Profilometry Analysis

Scanning electronic microscopy (SEM) and energy dispersive X-ray spectroscopy (EDS) were performed on both pristine and laser processed films of EGaIn and rGO@EGaIn, in order to compare the particles' morphology before and after laser treatment, as well as the corresponding elemental quantities. In these experiments, we kept laser parameters as 9 ns pulse width, 240 kHz and 50 mm/s, and then changed the laser fluence (by changing the power). As a reference, we first sintered a spray coated EGaIn nanoparticle film with no rGO, using 50% of laser power. Figure 3A shows EGaIn particles after deposition, without laser treatment. Figure 3B,C show the structures of sintered EGaIn at a fluence of 3.32 J/cm$^2$. The infrared laser is able to rupture the semiconductor gallium oxide shell, joins the EGaIn nanodroplets, and results in electrically conductive EGaIn traces.

Figure 3E,F shows pristine and laser scanned samples of rGO@EGaIn, respectively. As expected, the particles in GO coated EGaIn solution are less smooth and less reflective, compared to the EGaIn ones. The sample in Figure 3F was processed at the same laser fluence of samples shown in Figure 3B,C, but they have a very different morphology after laser treatment. Figure 3G shows the SEM image of the semitransparent, thinned rGO@EGaIn that was processed at higher laser fluence of 4.64 J/cm$^2$. The transparency seems to be due to both partial laser ablation, and laser thinning, as it will be discussed.

Figure 3H shows the EDS analysis of the samples and compares the atomic percentages of gallium, indium, carbon and oxygen for different samples from Z1-Z4, which confirms the above analysis. First, comparing the elemental analysis of Z1 and Z2, no significant changes can be seen, except the reduction of the oxygen content, as expected. The improved conductivity of the laser sintered samples at low laser fluence should be related to the partial reduction of GO and partial rupture of EGaIn nanoparticles.

The data also shows that the graphene encapsulation protects the $Ga_2O_3$ layer, from the laser generated heat. As it can

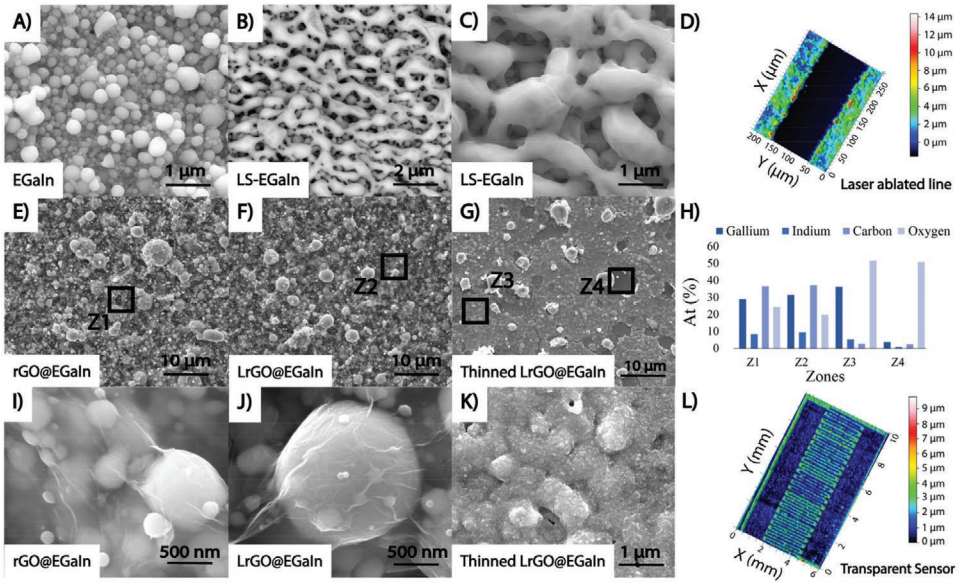


**Figure 3.** A) pristine film of EGaIn particles; B,C) laser sintered EGaIn particles showing the gallium oxide rupture and particle aggregation; D) 3D profilometer view of an ablated single line of rGO@EGaIn; E) pristine film of sprayed rGO@EGaIn particles; F) Laser reduced rGO@EGaIn particles at 50% power – as shown on Figure 2D); G) Laser thinned rGO@EGaIn at 70% power – as shown on Figure 2D); H) atomic percentages of the main elements on different areas (Z1-Z4) of the fabricated films; I,J) and K) are amplified views of E–G), respectively. L) 3D profilometer scan of a semitransparent interdigital electrode.

be seen in Figure 3B,C, when no GO is present, the $Ga_2O_3$ layer is fully ruptured by the same laser power that is applied to the sample of Figure 3F.

Referring to Figure 3G,H, when increasing further the laser fluence, the amount of carbon is significantly reduced (EDS analysis of the Z3 zone). This demonstrates the material thinning of the laser processed zones, as previously reported for laser induced graphene oxide monolayers.[35] In some zones (Z4), it is noticeable, that almost no material is left, which is confirmed by the EDS analysis. Therefore, the obtained transparency should be related both to the thinning of the sample and partial particle ablation, as it is visible in the Figure 3G.

Figures 3I,J shows a higher magnification of a graphene coated EGaIn particle in a rGo@EGaIn and a LrGO@EGaIn sample, respectively, where graphene sheets on the surface of EGaIn are clearly visible. Figure 3K shows a higher magnification of the laser thinned sample, where the microstructure has visible features that are smaller than the features seen in Figure 3I,J, and where the particles have joined each other. This should be the reason for the improved conductance of the thinned samples, compared to the non-sintered samples, despite the occurred material thinning.

Figure 3D depicts a 3D view of a single ablated line of rGO@EGaIn, obtained using an optical profilometer (Profilm3D, filmetrics). The middle zone is laser ablated. Figure 3L shows a 3D profilometer view of a semitransparent interdigitated electrode which can be used as a resistive or capacitive sensor. The laser reduced zone is considerably thinner (from ≈4 µm pristine film to <1 µm laser reduced part) and smoother than the areas which were not laser processed (see Table 2 in the Supporting Information).

### 2.3. XRD and Raman Spectroscopy

X-Ray diffraction (XRD) analysis in a range of $2\theta$ angle from ≈7 to ≈45° was performed on the as-sprayed films, with and without laser processing for better understanding the crystal phases of the synthesized composites. This way, three types of samples were analyzed: one with no laser irradiation, which we refer to as a pristine sample, and two others processed at 50% and 75% laser powers, which correspond to a non-transparent and a semitransparent sample, respectively. The results are shown in Figure 5A.

In the XRD pattern of the pristine sample, a sharp peak of GO in $2\theta \approx 9.89°$ is evident that related to the (0 0 1) crystal plane. Also, in this sample one wide peak in the $2\theta \approx 34.16°$ is visible that relates to the (1 1 1) plane of $\beta$-$Ga_2O_3$.

On the laser processed samples, peaks related to crystalline material are more visible, especially for the sample processed at 50% laser power (a non-transparent film). As expected, all the graphene oxide converted to reduced graphene oxide by applying laser treatment. Accordingly, the peak in $2\theta \approx 9.89°$ completely disappears and a wide peak at $2\theta \approx 25.47°$, with lower intensity compared to the GO, appears that is related to the (0 0 2) plane of rGO.

In the 50% laser power diffraction pattern, we detected monoclinic $\beta$-$Ga_2O_3$ (JCPDS No. 01-087-1901.) peaks at $2\theta$ values of: 18.88, 30.1, 30.4, 31.7, 33.4, 35.1, 37.5 and 38.4°, which correspond to (-2 0 1); (4 0 0); (-4 0 1); (-2 0 2); (-1 1 1); (1 1 1); (4 0 1) and (-3 1 1) planes respectively; as well as tetragonal indium (JCPDS No. 00-005-0642) peaks at $2\theta$: 33°, 36.4°, and 39.2° that correlated with (1 0 1); (0 0 2); (1 1 0) planes, respectively.

By increasing the laser power to 75%, most of the peaks that were clearly observed in the previous samples disappear, due to the thinning of the layers. In this diffraction pattern, we only detected one main plane of monoclinic $\beta$-$Ga_2O_3$ (1 1 1) at $2\theta \approx 35.1°$ and two main planes of tetragonal indium (1 0 1) and (1 1 0) at $2\theta \approx 33°$ and 39.2°, respectively.

These findings allow us to conclude that the MOPA laser induces local high temperature on the spray coated films, that further induces crystallinity of $Ga_2O_3$. Previously, only thermal sintering at >300 °C was reported to induce crystallinity of $Ga_2O_3$ in spray coated EGaIn nanoparticles, while laser sintered EGaIn remained amorphous.[27]

Raman spectroscopy has been used frequently as investigating tool for graphene and modified graphene.[36–44] Previous results have shown that pristine single-layer crystalline graphene exhibits two intense bands at ≈1585 and ≈2700 $cm^{-1}$, associated with the first- and second-order allowed Raman mode $E_{2g}$ ($C_{sp2}$-$C_{sp2}$ collective stretching) respectively, which are known as the G and 2D bands. Disorder, doping and chemical modification in graphene lead to the appearance of additional Raman bands, in particular the so-called D band, which is centered at ≈1350 $cm^{-1}$ and originates in the symmetry broken $A_{1g}$ breathing mode. These three bands are observed in GO, but in this case the 2D band is of low intensity and broad. Compared to neat graphene, changes in the width of these three bands occur for GO in result of the increasing defect concentration associated with the oxidation. In GO, the 2D spectral region is complicated by the appearance of additional bands that correspond to the second-order modes (both overtones and combination tones) associated with the D′, D″ and D* bands mentioned below and also with the G+D combination,[36,40] and recent reports have shown that the 2D band of highly disordered GO (and graphenes in general) strongly reduces its intensity and appears only as a bump in the spectral baseline of the Raman spectra of these materials.[39]

Three additional weak bands are also present in GO Raman spectra, all of them reflecting disorder in the material in some extent: the D′ band, observed at ≈1620 $cm^{-1}$, which has been attributed to a disorder-induced phonon mode due to crystal defects,[36,41,42] the D* band, located between 1150 and 1200 $cm^{-1}$, related to graphitic lattice disorder at the edges of networks,[36,43] and the D″ band, appearing between 1500 and 1550 $cm^{-1}$, which is related to amorphous phases.[36,43]

The two sets of bands described above (G, D and 2D in the one side, and D′, D″ and D* in the other sine) can be used to evaluate both the degree of reduction and the degree of disorder of GO samples. Indeed, it is well established that the relative intensity of the D band with respect to the G band ($I_D/I_G$) is a good parameter to estimate the degree of defects in the graphene network,[36,41] while the width of the D and G bands decreases upon reduction of GO and increases with the increase of the defects.[36,41] $I_D/I_G$ gives also an insight into the reduction process of GO, since the removal of the oxygen functional groups of GO may create imperfections within

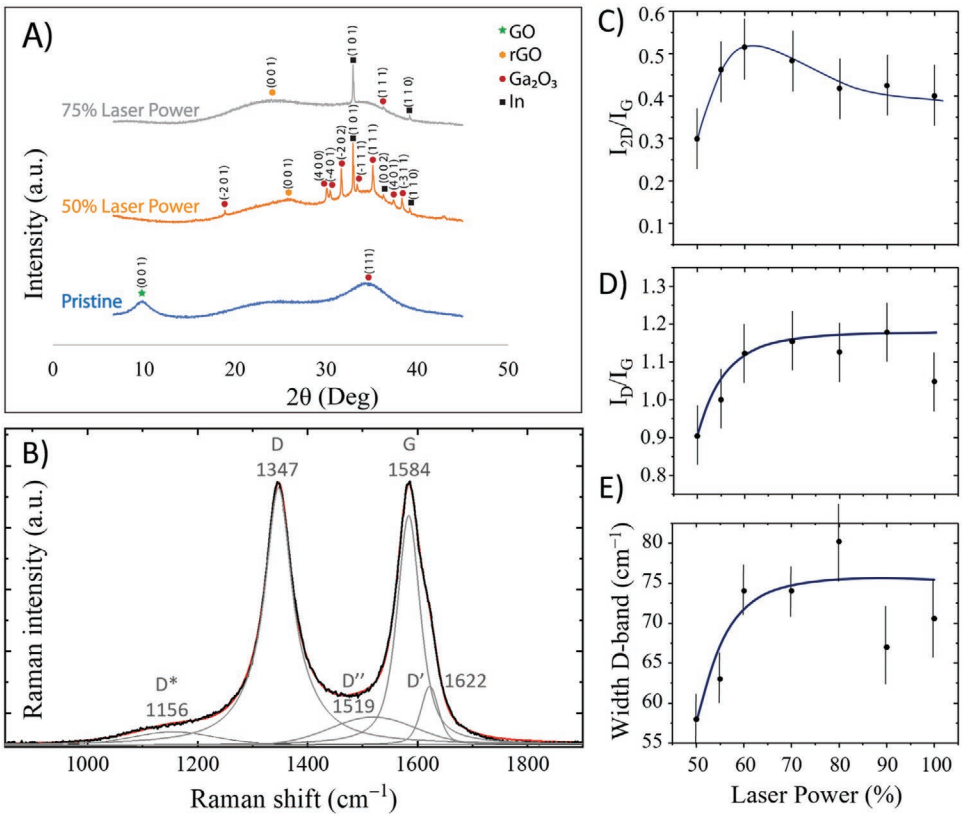


**Figure 4.** A) XRD diffraction patterns of spray coated and laser processed GO@EGaIn films, with the amorphous and crystalline peaks detected for each sample. B) General profile of the obtained Raman spectra of the investigated samples in the 1000–1800 cm–1 spectral range, with position of the maxima and the band assignment. The black bold spectrum is the experimental data; the five grey curves are the fitted bands, whose sum curve corresponds to the red line. Plots of C) $I_{2D}/I_G$ and of D) $I_D/I_G$, as well as the full-width-at-half-width of the E) D band for the spectra of the studied samples as a function of the power of the laser. The bars are indicative of the expected error and include a statistical component and the experimental error in measuring the band intensities and bandwidths.

the carbon network. Besides, as mentioned above, the $I_{2D}/I_G$ ratio is also an indicator of the degree of disorder and level of oxidation of graphene, reducing its value with the increase of these two properties. These spectral indicators associated with the G, D and 2D bands were used in the present study to characterize the rGO samples that were produced using different laser power. The spectral parameters of the low intensity bands, in particular D″ and D*, could also have been used for this objective, since the position of the D″ and D* peaks has been shown to shift to lower and higher wavenumber values, respectively, when oxygen content in GO decreases,[36] and a decrease of the intensity ratio $I_D''/I_G$ and of the width of the D″ band has also been shown to correlate directly with the degree of crystallinity of the material.[36] However, the fact that these bands are of low intensity and appear extensively overlapped by the intense G and D bands discouraged their use in favor of the analyses made based on the intense G, D, and 2D bands.

**Figure 4**B shows the general profile of the obtained Raman spectra of the investigated samples, where the component bands were obtained by curve fitting following the procedure described in Ref. [36]. In the 1000–1800 $cm^{-1}$ spectral range, all G, D, G′, G″ and G* bands are observed at the expected frequencies. In the 2D spectral range, the spectra present the above-described profile, with several bands, from which that observed at ≈2700 $cm^{-1}$ corresponds to the 2D mode.

Figure 4C–E) presents the plots of $I_{2D}/I_G$ and of $I_D/I_G$, as well as the full-width-at-half-width of the D band for the spectra of the studied samples as a function of the power of the laser. As described above these spectral parameters are indicators of the degree of disorder and level of oxidation of the samples.

From Figure 4C, one can see that the $I_{2D}/I_G$ ratio reaches a maximum for the laser power of ≈60% indicating that the reduction of the GO increases with the power of the laser. After this value of laser power the $I_{2D}/I_G$ ratio start to decrease due to the effect of disorder (higher amount of defects) increase, which tends to increase the intensity ratio. Note that 60% power is the threshold in which samples start to show some transparency, which seems to be related with material thinning. For laser powers of ca. 80% or greater the $I_{2D}/I_G$ ratio reaches a nearly constant value, a result that combined with the data shown in Figure 4D,E seems to indicate that for laser powers greater than ca. 80% the degrees of reduction of the GO and of the disorder are not significantly different. Indeed, the plot shown in Figure 4D, of $I_D/I_G$ as a function of the laser power, increase until a laser power of ca. 80%, expressing the simultaneous increase of the degrees of reduction of the GO and of disorder, and attains a plateau for values of the laser power

equal or above ca. 80%, while the observation of the same type of profile in the case of the plot shown in Figure 4E, of the full-width-at-half-width of the D band as a function of the laser power, seems to indicate that the influence of the disorder in this spectral parameter supersedes that due to the increase of the GO reduction degree. Note also that the measurement of both the intensity and width of the D band (and also of the G band) for higher laser power values could be anticipated to show larger experimental errors, due to the intensification of the D′, D″ and D* bands with the increase of the disorder, as observed experimentally (particularly noticeable in the case of the width data). In the case of the error in the measurement of the intensity of the G band, this fact may also affect the calculated values of the $I_{2D}/I_G$ ratio for laser powers of 80 and 90%, which may be somewhat overestimated (nevertheless, not affecting the conclusion presented above taken based on this intensity ratio).

### 2.4. High Resolution and Scalable Laser Patterning

In order to show the simplicity, versatility, scalability, and patterning resolution of the used technique, different structures were laser processed using rGO@EGaIn films. Only the laser power was changed in the experiments now discussed. The pulse width was fixed at 9 ns, the beam frequency at 240 kHz, and the speed at 50 mm/s. The hatch spacing used was 50 µm.

**Figure 5**Ai shows a full array of 18 interdigitated electrodes made of LrGO@EGaIn. This type of geometry is widely used both as resistive and capacitive sensors, and supercapacitors. The process is, therefore, highly scalable since it took less than two minutes to make the electrodes. Figure 5Aii shows a close view of one of the opaque electrodes (the darker areas are the ones irradiated by the laser). A glass with the array of electrodes was tape attached to a visor (Figure 5viii)); and to a PMMA substrate for human breath detection at a distance of 40 cm (Figure 5v)). We tested 2 devices for the detection of human breath, one opaque (i.e. reduced with low laser power), and one semitransparent, in order to show device functionality, regardless of transparency. We used silver ink to attach the wires to our sensors before acquiring the signals. In this case, we exploited the change in the resistance of rGO@EGaIn zones between the laser reduced electrodes, when subjected to the breath. This resistance change cycle is according to the breath cycle (inhale-exhale). The results can be seen in the graphs shown in Figure 5Aiii,iv,vi,vii. Both opaque and semitransparent devices worked with similar performance.

In order to show the potential of the laser technique to process larger areas, a world map was laser patterned on top of a 10 $cm^2$ PMMA substrate (Figure 5B)). An additional video of the real time lasering of the sample is shown on video S4 from the Supporting Information. Here the maximum process able area is 10 $cm^2$, with a stationary laser head. This can be easily extended to larger areas, by installation of the laser on a X-Y table. Figure 5C) demonstrates a semitransparent conductor with interfaced LEDs, produced with the developed technique, in which LEDs are lighted, while the background material is nearly imperceptible (Video S4 – Supporting Information). The brighter circuit lines shown in the picture are the fully ablated areas, working as a cleaning tool for circuit integration.

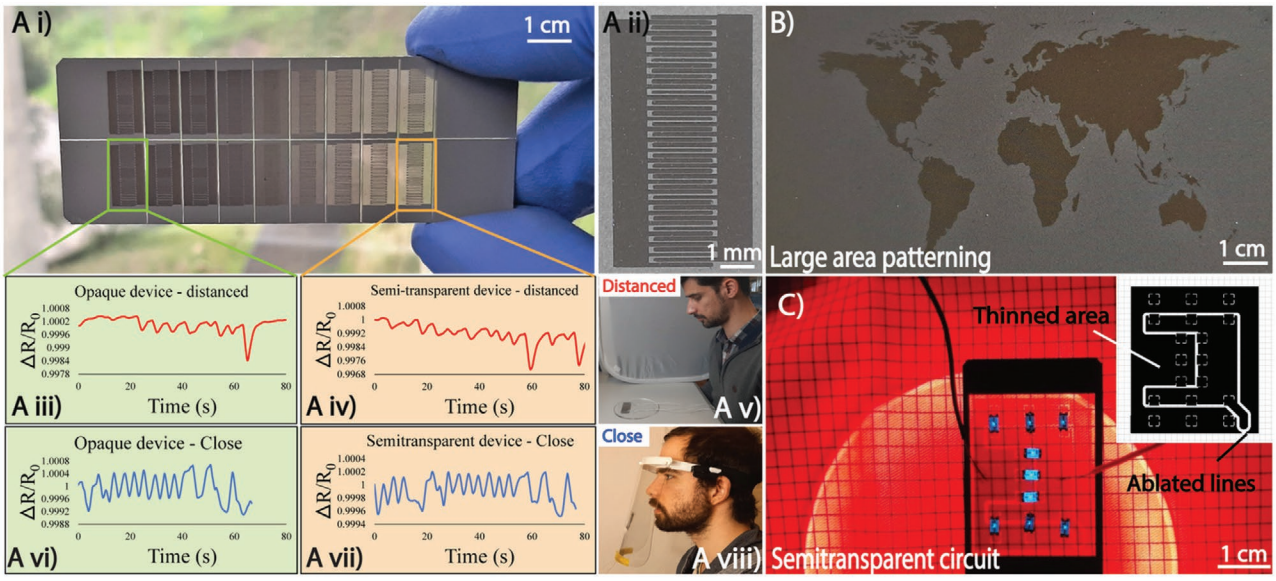


**Figure 5.** Ai) Array of 18 interdigital electrodes laser patterned over glass, showing device's scalability; some are semitransparent (right), some are (left). The laser powers used to build the array varied between 50–85%. In between the electrodes, lines were ablated to insulate them from each other. Aii) a close look at the high resolution, opaque laser patterned interdigital electrode made of LrGO@EGaIn – the real dimensions can be seen on Figure 3L. Aiii) Resistance variation of an opaque sensor tested at a distance of 40 cm from the breath source; Aiv) Resistance variation of a semitransparent sensor tested at a distance of 40 cm from the breath source; Av) Setup used to test the device at a distance of 40 cm from the breath source; Avi) Resistance variation of an opaque sensor tested with the face shield on (close to breath source); Avii) Resistance variation of a semitransparent sensor tested with the face shield on (close to breath source); Aviii) Setup used to test the device with the face shield (close to the breath source). B) A large area laser patterned world map on PMMA. C) A semitransparent conductive circuit used to light on a few LEDs.

### 2.5. Conclusions and Further Work

In this letter, we demonstrated for the first time the production of electrically conductive and semitransparent LrGO@EGaIn electrodes, based on the laser patterning of rGO@EGaIn. This was performed using a 1064 nm wavelength MOPA laser. Laser reduction of sprayed rGO@EGaIn particles enhances their electrical conductivity without extreme morphology changes, which were probed by different techniques including SEM, EDS, XRD, and Raman spectroscopy. This partially reduced GO shell protects the $Ga_2O_3$ layer around the EGaIn droplet from rupture at lower laser fluence. Nevertheless, the laser reduction at low powers is still able to make the films conductive. Unexpectedly, we found that at higher laser fluence, film thinning of rGO@EGaIn results in semitransparent conductor, which might enable future applications in optoelectronics. SEM microcopy and EDS analysis showed that EGaIn droplets are coated by GO sheets.

We also demonstrated a visually imperceptible circuit with some LEDs, and an ultrasensitive respiration sensor fabricated with two laser patterned interdigitated electrodes, which is able to detect the human breath from 40 cm distance.

In summary, the technique described in the present investigation provides a facile method for the fabrication of laser reduced graphene oxide decorated EGaIn particles based conductive, and semitransparent electrodes. Both spray coating and laser patterning techniques are low-cost, rapid and scalable. Custom designed electrodes with high resolution can be prepared in a few seconds using this approach. Future work includes investigating the use of other types of lasers for improving the conductivity or transparency of the electrodes and investigating applications of this technique in the fields of thin-film electronics, gas and humidity sensors, and energy devices.

## 3. Experimental Section

*Materials and Equipment*: Graphene oxide water dispersion (0.4 wt%) was ordered from Graphenea. Gallium and indium were ordered from Rotometals. Acetic acid was ordered from Carlo Erba Reagents. To prepare the gallium based liquid metal, ≈75 g of previously melted gallium were mixed with ≈25 g of indium and allowed to alloy overnight inside of an oven at 250 °C.

The glass slides used as substrates were ordered from Normax. For the large area coatings, 10 $cm^2$ acrylic cookies (5 mm thick) were laser cut using a VLS3.50 $CO_2$ laser from Universal Laser Systems.

A Honsell 130 spray gun, with a 0.5 mm nozzle diameter, was used to deposit the GO@EGaIn suspension onto the desired substrates.

The laser system used was a 1064 nm MOPA fiber laser from JPT, with operating pulse widths in the 6–250 ns range, and maximum output power of 20 W. The laser spot size is ≈40 µm. All sheet resistance measurements were performed using a Fluke 45 Dual Display Multimeter. The films' thicknesses were characterized with a 3D profilometer from filmetrics. The transmittance results were obtained using a LABTRONICS spectrophotometer. SEM and EDS analysis were made using a FEI Quanta 400 FEG-E-SEM/EDAX Genesis X4M.

*Ink's Synthesis and Coating*: Graphene oxide suspension was used as received in all the experiments described. In a 30 ml vial, 20 ml of the commercial GO solvent were dispensed using a pipette. EGaIn (1 g) and 0.1 M acetic acid (1 ml) were added to the GO solution. Finally, the vial was protected with parafilm, and a hole was punctured on top of it, serving as the entrance for the tip of the sonicator. The vial was then placed inside a 1 litter vial containing an ice bath, to keep the sample cooled down during the sonication. After having the mixture centrally placed inside the 1 litter vial, sonication took place at 60% amplitude for 20 min, under a temperature below 20 °C. The result is a paste in which a slight phase separation can be seen. In order to promote a further homogeneous dispersion, the sonicated material was subjected to 3 min of rotary mixing at 2000 rpm, promoting a liquid phase dark grey ink (video S2 in the Supporting Information).

The dark brown/grey suspension was then pipetted into the spray gun compartment, while the glass slides were placed on top of a hot plate at 60 °C, temperature at which the films were prepared, to allow faster drying of the ink. Around 2 ml of ink is used for each glass slide of $7.5 \times 2.5$ $cm^2$. For the acrylic substrates, a similar apparatus is used with adjustments in the ink volume for a larger area. For the SEM and EDS analysis, a similar approach was done on thinner glass slides of 2 $cm^2$, in which half of the slide was laser processed and the other half was kept in its pristine state. The spray gun was subjected to a constant pressure of 4 psi throughout the coating process.

Another ink of EGaIn only was prepared for SEM analysis. In this case, 1 g of EGaIn was added to 20 mL of 2-propanol and sonicated in the same conditions as described for the GO@EGaIn ink. The spray coating was also done on glass following the same protocol as described previously for the GO@EGaIn ink.

*Human Breath Detection*: All participants agreed to share their personal data for the purpose of the study. The laser patterned interdigital electrodes on glass were wired with the assistance of a lab-made soft conductive paste based on SIS polymer and silver flakes. The wires were connected to 2 Arduino boards and using a 24 bits ADC with a Resistor in series of 10 kΩ and 5 V applied, the change in the device's resistance was measured. Video S1 (Supporting Information) shows the real time acquisition of the data.

*X-Ray Diffraction*: XRD analysis was conducted using a D8 Advance Bruker diffractometer. The diffractograms were obtained in the Bragg-Brentano geometry. The diffraction angle was 0.2°, with Soller slits of 2.5° in the input and output beams.

*Raman Spectroscopy*: Raman spectra were recorded with 0.5 $cm^{-1}$ spectral resolution in a micro-Raman Horiba LabRam Evolution system and were automatically corrected for the spectral response of the apparatus. Excitation was provided by a solid-state laser at $\lambda = 532$ nm focused on the sample onto a sub-micron spot using a x100 objective. The laser power was set at values within the range 0.15 – 1.25 mW, which were low enough to avoid local heating and damaging of the sample but permitted to obtain good signal-to-noise ratio in a reasonable acquisition time. The smallest laser powers were used for the thinnest samples studied, which correspond to those prepared with the highest laser powers during GO reduction. The typical acquisition time of one Raman spectrum was 10 s, with 30 accumulations. The wavenumber calibration was performed using the characteristic Si wafer band at 520.5 $cm^{-1}$.

## Supporting Information

Supporting Information is available from the Wiley Online Library or from the author.

## Acknowledgements

A.C. and A.L.S. contributed equally to this work. This work was partially supported by WoW – Wireless biOmonitoring stickers and smart bed architecture: to Wards Untethered Patients (Ref: Centro-01-0247-FEDER-045931); MATIS – Materiais e Tecnologias Industriais Sustentáveis (Ref: Centro 2020 000014 MATIS 2020); and Dermotronics (PTDC/EEIROB/31784/2017), financed by the EU structural & investment

 

Funds (FEEI) through operational program of the center region, through FCT. Access to the experimental facilities of TAIL-UC facility funded under QREN-Mais Centro project ICT_2009_02_012_1890 is gratefully acknowledged, along with Dr. José Paixão's work, who conducted the XRD analysis. The CQC was funded by the FCT through the projects UIDB/QUI/00313/2020 and UIDP/QUI/00313/2020.

## Conflict of Interest

The authors declare no conflict of interest.

## Data Availability Statement

The data that support the findings of this study are available from the corresponding author upon reasonable request.

## Keywords

graphenes, liquid metals, microcomposites, MOPA laser writing, transparent electronics

Received: September 30, 2021
Published online: October 27, 2021

[1] S. K. Tiwari, S. Sahoo, N. Wang, A. Huczko, *Adv. Mater. Devices* **2020**, *5*, 10.
[2] O. C. Compton, S. T. Nguyen, *Small* **2010**, *6*, 711.
[3] J. K. Wassei, R. B. Kaner, *Mater. Today* **2010**, *13*, 52.
[4] H. Kashani, Y. Ito, J. Han, P. Liu, M. Chen, *Sci. Adv.* **2019**, *5*, eaat6951.
[5] F. Alotaibi, T. T. Tung, M. J. Nine, C. J. Coghlan, D. Losic, ACS Appl, *Nano Mater.* **2018**, *1*, 2249.
[6] A. Khan, M. Jawaid, D. Inamuddin, A. M. Asiri, A. Khan, *Nanocarbon and its Composites: Preparation, Properties and Applications*, 1st ed., Woodhead Publishing **2018**.
[7] J. Y. Kim, H. Lim, S. Y. Lee, C. Song, J. W. Park, H. H. Shin, D. K. Lim, D. W. Moon, *ACS Appl. Mater. Interfaces* **2019**, *11*, 27153.
[8] R. You, Y. Q. Liu, Y. L. Hao, D. D. Han, Y. L. Zhang, Z. You, *Adv. Mater.* **2020**, *32*, 1901981.
[9] Y. Chyan, R. Ye, Y. Li, S. P. Singh, C. J. Arnusch, J. M. Tour, *ACS Nano* **2018**, *12*, 2176.
[10] M. F. El-Kady, V. Strong, S. Dubin, R. B. Kaner, *Science* **2012**, *335*, 1326.
[11] T. Liu, P. Sen, C. J. Kim, *J. Microelectromech. Syst.* **2012**, *21*, 443.
[12] C. Yang, J. He, Y. Guo, D. Zhao, X. Hou, J. Zhong, S. Zhang, M. Cui, X. Chou, *Mater. Des.* **2021**, *201*, 109508.
[13] A. R. Jacob, D. P. Parekh, M. D. Dickey, L. C. Hsiao, *Langmuir* **2019**, *35*, 11774.
[14] J. Zhu, Y. Wu, X. Huang, L. Huang, M. Cao, G. Song, X. Guo, X. Sui, R. Ren, J. Chen, *Nano Energy* **2019**, *62*, 883.
[15] Y. Lin, J. Genzer, M. D. Dickey, *Adv. Sci.* **2020**, *7*, 2000192.
[16] D. F. Fernandes, C. Majidi, M. Tavakoli, *J. Mater. Chem. C* **2019**, *7*, 14035.
[17] M. Tavakoli, M. H. Malakooti, H. Paisana, Y. Ohm, D. Green Marques, P. Alhais Lopes, A. P. Piedade, A. T. de Almeida, C. Majidi, *Adv. Mater.* **2018**, *30*, 1801852.
[18] P. A. Lopes, H. Paisana, A. T. Almeida, C. Majidi, M. Tavakoli, A. T. De Almeida, C. Majidi, M. Tavakoli, *ACS Appl. Mater. Interfaces* **2018**, *10*, 38760.
[19] A. F. Silva, H. Paisana, T. Fernandes, J. Góis, A. Serra, J. F. J. Coelho, A. T. de Almeida, C. Majidi, M. Tavakoli, *Adv. Mater. Technol.* **2020**, *5*, 2000343.
[20] R. Rocha, P. Lopes, A. T. de Almeida, M. Tavakoli, C. Majidi, in *2017 IEEE/RSJ International Conference on Intelligent Robots and Systems (IROS)*, Vancouver, BC, Canada **2017**, pp. 3734–3738, https://doi.org/10.1109/IROS.2017.8206222.
[21] R. P. Rocha, P. A. Lopes, A. T. de Almeida, M. Tavakoli, C. Majidi, *J. Micromech. Microeng.* **2018**, *28*, 034001.
[22] J. Alberto, C. Leal, C. Fernandes, P. A. Lopes, H. Paisana, A. T. de Almeida, M. Tavakoli, *Sci. Rep.* **2020**, *10*, 5539.
[23] C. Leal, P. A. P. A. Lopes, A. A. Serra, J. F. J. J. F. J. J. Coelho, A. T. A. T. A. T. De Almeida, M. Tavakoli, *ACS Appl. Mater. Interfaces* **2020**, *12*, 3407.
[24] N. Kazem, T. Hellebrekers, C. Majidi, *Adv. Mater.* **2017**, *29*, 1605985.
[25] P. Alhais Lopes, D. Félix Fernandes, A. F. Silva, D. Green Marques, A. T. de Almeida, C. Majidi, M. Tavakoli, *ACS Appl. Mater. Interfaces* **2021**.
[26] S. Liu, M. C. Yuen, E. L. White, J. W. Boley, B. Deng, G. J. Cheng, R. Kramer-Bottiglio, *ACS Appl. Mater. Interfaces* **2018**, *10*, 28232.
[27] S. Liu, S. N. Reed, M. J. Higgins, M. S. Titus, R. Kramer-Bottiglio, *Nanoscale* **2019**, *11*, 17615.
[28] R. Abbasi, M. Mayyas, M. B. Ghasemian, F. Centurion, J. Yang, M. Saborio, F. M. Allioux, J. Han, J. Tang, M. J. Christoe, K. M. Mohibul Kabir, K. Kalantar-Zadeh, M. A. Rahim, *J. Mater. Chem. C* **2020**, *8*, 7805.
[29] M. gu Kim, D. K. Brown, O. Brand, *Nat. Commun.* **2020**, *11*, 1002.
[30] M. A. Creighton, M. C. Yuen, N. J. Morris, C. E. Tabor, *Nanoscale* **2020**, *12*, 23995.
[31] Y. Wang, S. Wang, H. Chang, W. Rao, *Adv. Mater. Interfaces* **2020**, *7*, 2000626.
[32] M. G. Saborio, S. Cai, J. Tang, M. B. Ghasemian, M. Mayyas, J. Han, M. J. Christoe, S. Peng, P. Koshy, D. Esrafilzadeh, R. Jalili, C. H. Wang, K. Kalantar-Zadeh, *Small* **2020**, *16*, 1903753.
[33] X. Chen, L. Zhang, S. Chen, *Synth. Met.* **2015**, *210*, 95.
[34] E. Kymakis, E. Stratakis, M. M. Stylianakis, E. Koudoumas, C. Fotakis, in *Thin Solid Films*, Vol. *520*, **2011**, pp. 1238–1241.
[35] H. G. Hee, C. Seung Jin, K. Eun Sung, G. Fethullah, L. Il Ha, L. S. Won, L. S. Young, L. Seong Chu, J. Hae Kyung, J. Mun Seok, L. Y. Hee, *ACS Nano* **2011**, *5*, 263.
[36] S. Claramunt, A. Varea, D. López-Díaz, M. M. Velázquez, A. Cornet, A. Cirera, *J. Phys. Chem. C* **2015**, *119*, 10123.
[37] Ado Jorio, Riichiro Saito, Gene Dresselhaus, Mildred S. Dresselhaus, *Raman Spectroscopy in Graphene Related Systems*, xxxx, Weinheim **2011**.
[38] S. Reich, C. Thomsen, *Trans. R. Soc. A.* **2004**, *362*, 2271.
[39] E. H. M. Ferreira, M. V. O. Moutinho, F. Stavale, M. M. Lucchese, R. B. Capaz, C. A. Achete, A. Jorio, *Phys. Rev. B* **2010**, *82*, 125429.
[40] X. Díez-Betriu, S. Álvarez-García, C. Botas, P. Álvarez, J. Sánchez-Marcos, C. Prieto, R. Menéndez, A. de Andrés, *J. Mater. Chem. C* **2013**, *1*, 6905.
[41] S. Vollebregt, R. Ishihara, F. D. Tichelaar, Y. Hou, C. I. M. Beenakker, *Carbon* **2012**, *50*, 3542.
[42] X. Zhao, Y. Ando, *Jpn. J. Appl. Phys., Part 1* **1998**, *37*, 4846.
[43] A. Sadezky, H. Muckenhuber, H. Grothe, R. Niessner, U. Pöschl, *Carbon.* **2005**, *43*, 1731.
[44] V. Scardaci, G. Compagnini, *C 2021* **2021**, *7*, 48.